Journal of Environmental Chemical Engineering 11 (2023) 109407

Contents lists available at ScienceDirect

Journal of Environmental Chemical Engineering

journal homepage: www.elsevier.com/locate/jece

C≡N vacancy engineering of Prussian blue analogs for the advanced oxygen evolution reaction

Wenhao Deng [a,1], Baochai Xu [a,1], Qiangqiang Zhao [a], Song Xie [a], Weihong Jin [b], Xuming Zhang [c], Biao Gao [c], Zhitian Liu [a], Zaenab Abd-Allah [d], Paul K. Chu [e], Xiang Peng [a,*]

[a] Hubei Key Laboratory of Plasma Chemistry and Advanced Materials, Hubei Engineering Technology Research Center of Optoelectronic and New Energy Materials, Wuhan Institute of Technology, Wuhan 430205, China
[b] Institute of Advanced Wear & Corrosion Resistant and Functional Materials, Jinan University, Guangzhou 510632, China
[c] State Key Laboratory of Refractories and Metallurgy and Institute of Advanced Materials and Nanotechnology, Wuhan University of Science and Technology, Wuhan 430081, China
[d] Department of Engineering, Manchester Metropolitan University, John Dalton Building, Manchester M15 6BH, United Kingdom
[e] Department of Physics, Department of Materials Science and Engineering, and Department of Biomedical Engineering, City University of Hong Kong, Tat Chee Avenue, Kowloon, Hong Kong, China

ARTICLE INFO

Editor: V. Victor

Keywords:
C≡N vacancy
Prussian blue analogs (PBAs)
Oxygen evolution reaction
Water splitting
Hydrogen production

ABSTRACT

Hydrogen production by electrocatalytic water splitting suffers from the sluggish kinetics of the oxygen evolution reaction (OER) and large power consumption and hence, efficient OER electrocatalysts are required to enhance the energy conversion efficiency. Vacancies can create active unsaturated coordination, regulate the electronic structure, and enhance the charge transfer efficiency to improve both the intrinsic and extrinsic catalytic activities. This work aims to construct an efficient OER electrocatalyst through precise control of the C≡N vacancies ($V_{C\equiv N}$) in NiFe- and NiCo-Prussian blue analogs (PBAs) leading to outstanding OER characteristics and improved energy conversion efficiency. The amount of $V_{C\equiv N}$ has been regulated precisely via thermal treatment. The electronic interactions occur between Ni and Fe sites during the introduction of $V_{C\equiv N}$. As a result, the synergistic effects of Ni-Fe electronic interactions and $V_{C\equiv N}$ lead to outstanding OER characteristics such as a small overpotential of 270 mV to achieve a high current density of 50 mA cm^{-2} as well as excellent stability over 80 h, which are better than those of the pristine PBAs electrocatalyst. The results demonstrate a precise strategy to produce $V_{C\equiv N}$ in PBAs-based electrocatalysts for advanced OER and efficient hydrogen production.

1. Introduction

Clean and sustainable energy is essential to combating climate change. Electrochemical water splitting is a promising means to produce pure hydrogen for clean energy generation [1–3]. Water electrolysis consists of the hydrogen evolution reaction (HER) on the cathode and oxygen evolution reaction (OER) on the anode and the slow kinetics of OER are usually the bottleneck that limits the energy conversion efficiency [4,5]. Noble metal-based catalysts such as IrO_2 and RuO_2 have been applied to facilitate OER but their high costs and low reserves are huge barriers against commercial adoption [6,7]. Therefore, economical and high-activity non-noble metal-based electrocatalysts are imperative to advanced OER.

Abundant metals such as Ni, Co, Fe and their compounds have been proposed to enhance OER. For example, Ni and its compounds such as Ni metals [8,9], $NiSe_2$ [10,11], NiO [12,13], and NiFeO [14] can drive OER at low overpotentials. For instance, an electrocatalyst consisting of Ni-FeO_x and $FeNi_3$ has been prepared on nickel foam (Ni-FeO_x/Fe-Ni_3/NF) which requires 269 mV to yield a current density of 50 mA cm^{-2} in OER and shows good stability over 200 h [14]. The crystal structure of the electrocatalysts is also crucial to the performance. The Prussian blue analogs (PBAs) are considered as promising electrocatalysts for OER due to their tunable structure and composition [15]. PBAs are perovskite-type materials with the general formula of $A_xM_1[M_2(C\text{-}N)_6]_y{\cdot}mH_2O$, where A stands for an alkali metal such as Na and K, M_1 and M_2 are metals such as Ni, Co, Fe, etc. [16–18]. Bimetallic

* Corresponding author.
E-mail address: xpeng@wit.edu.cn (X. Peng).
[1] These authors contributed equally to this work.

https://doi.org/10.1016/j.jece.2023.109407
Received 2 December 2022; Received in revised form 27 January 2023; Accepted 29 January 2023
Available online 31 January 2023

electrocatalysts composed of nickel and iron have been reported to have good OER activity [19,20]. For example, Wu et al. have prepared bimetallic Ni-Fe selenide from NiFe-PBAs with an optimized electronic structure that exhibits synergistic effects between Ni and Fe and has good OER characteristics [20]. However, the C≡N species which account for a larger proportion of PBAs do not play a significant role in OER.

Generally, PBAs are composed of M_2–C≡N–M_1 units with strong C≡N bonds and relatively weak M_2–C and M_1–N bonds [21]. Hence, it is possible to break the M_2–C and M_1–N bonds directionally with moderate energy to produce C≡N vacancies ($V_{C≡N}$) in PBAs. Vacancy/defect engineering is in fact an effective strategy to generate active unsaturated coordination [22,23], regulate the electronic structure [24–26], and enhance the charge transfer efficiency [27] to improve both the intrinsic and extrinsic catalytic activities. $V_{C≡N}$ have been created in PBAs by a plasma treatment [21,28]. Yu et al. have studied the OER characteristics of $V_{C≡N}$ mediated PBAs, which exhibit a low overpotential of 283 mV at 10 mA cm^{-2} which is better than those of the original PBAs and previously reported OER electrocatalysts with vacancies [21]. Lai et al. have constructed $V_{C≡N}$ in PBAs by N_2 plasma processing and shown high-efficiency OER activity with a low overpotential (270 mV at 50 mA cm^{-2}) and excellent performance for oxygen reduction reaction with a positive potential of 0.89 V at 5 mA cm^{-2} [28]. However, plasma processing typically requires a complex apparatus and bond breaking tends to be random. Therefore, a more precise and easier technique to produce $V_{C≡N}$ in PBAs is important albeit challenging.

Herein, a strategy of precisely regulating the $V_{C≡N}$ in NiFe-PBAs *via* a mild thermal treatment is described, as illustrated in Scheme 1. The amount of $V_{C≡N}$ in NiFe-PBAs can be adjusted precisely by controlling the treatment temperature. NiFe-PBAs with different $V_{C≡N}$ concentrations can be prepared and electronic interactions between Ni and Fe sites are introduced. The synergistic effects rendered by the Ni-Fe electronic interactions and $V_{C≡N}$ give rise to outstanding OER characteristics such as a small overpotential of 270 mV to reach a current density of 50 mA cm^{-2} in addition to good stability of 80 h, which are better than those of the pristine PBAs electrocatalysts. Moreover, this mild thermal treatment strategy can be extended to other PBAs-based electrocatalysts (NiCo-PBAs).

2. Experimental details

2.1. Materials preparation

2.4 mmol $NiCl_2$ and 3.6 mmol $Na_3C_6H_5O_7{\cdot}2\,H_2O$ were dissolved in 80 mL of deionized water (DW) to obtain solution A and then 1.6 mmol $K_3Fe(CN)_6$ was dissolved in 80 mL of DW water to produce solution B. Solution A was added to solution B dropwise under stirring. A piece of clean carbon cloth (CC, 5 ×6 cm^{-2}) was immersed in the mixture for 24 h and then rinsed with DW and ethanol several times before vacuum drying. The product was designated as NiFe-PBAs.

To regulate the C≡N ligands, NiFe-PBAs were thermally treated at 200, 250, and 300 °C in a tube furnace under N_2 at a rate of 5 °C min^{-1} for 2 h, respectively. The products were designated as PBAs-200, PBAs-250, and PBAs-300, where the numbers indicate the treatment temperature. The mass loading of NiFe-PBAs-based electrocatalysts on the CC is ~0.2 mg cm^{-2}. NiCo-PBAs were prepared by the same protocol as NiFe-PBAs except for replacing $K_3Fe(CN)_6$ with $K_3Co(CN)_6$. NiCo-PBAs were thermally treated in a tube furnace under N_2 to produce C≡N deficient NiCo-PBAs (NiCo-PBAs-V).

2.2. Materials characterization

A scanning electron microscope (SEM, FEI/Philips XL30 Esem-FEG) and a transmission electron microscope (TEM, Talos F200S G2) were used to characterize the morphology of the samples. The crystal structure of the samples was determined by the X-ray diffraction (XRD, LabX-6100, Shimadzu) and high-resoltuion TEM (HR-TEM). Raman scattering (HR RamLab) was conducted to analyze the chemical bonding and X-ray photoelectron spectroscopy (XPS, Thermo Scientific K-Alpha, Thermo Fisher) with monochromatic Al Kα X-ray was performed to determine the chemical states referenced to the C 1 *s* peak at 284.8 eV.

2.3. Electrochemical assessment

The electrochemical measurements were carried out in 1 M KOH on the CHI 660E electrochemical workstation (Shanghai CH Instrument, China). The typical three-electrode system consisted of a graphite rod, saturated calomel electrode (SCE), and PBAs modified CC as the counter electrode, reference electrode, and working electrode, respectively. All the potentials in OER were *iR* corrected and referenced to the reversible hydrogen electrode (RHE) according to Nernst equation $E(\mathrm{RHE}) = E(\mathrm{SCE}) + 0.242 + 0.059 \times \mathrm{pH}$. The pH of 1 M KOH solution was measured to be 13.62 by a pH meter (FE, Mettler Toledo). Linear sweep voltammetry (LSV) was performed at a scanning rate of 5 mV s^{-1} to obtain the polarization curves. The Tafel slopes were plotted as overpotentials (V) *vs.* log currents (log|*j*|) based on the polarization curves. The electrochemical active surface area (ECSA) was obtained by measuring the electrochemical double-layer capacitance (C_{dl}) based on the cyclic voltammetry (CV) curves at different scanning rates of 10–100 mV s^{-1}. Electrochemical impedance spectroscopy (EIS) was carried out at an initial potential of 0.5 V *vs.* SCE. The long-term durability was evaluated by chronoamperometry for more than 80 h and O_2 production was measured by the water displacement method.

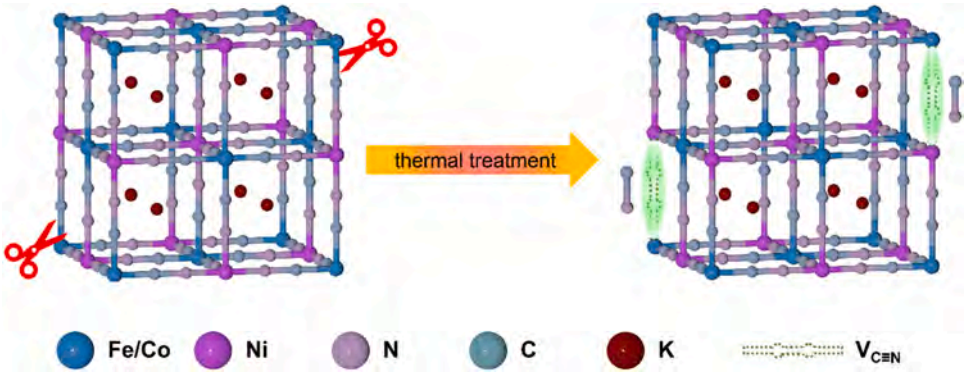

Scheme 1. C≡N vacancy engineering of PBAs.

3. Results and discussion

3.1. Structure and composition study

NiFe-PBAs prepared on CC by heterogeneous nucleation with a chelating agent [29,30] contain Fe–C≡N–Ni units with strong C≡N bonds and relatively weak Fe–C and Ni–N bonds [21]. The thermal treatment cleaves the Fe–C and Ni–N bonds in the Fe–C≡N–Ni units due to the higher activation barrier of cleaving the C≡N bonds as illustrated in Scheme 1. The generated C≡N then moves away from the PBAs lattices to form the $V_{C\equiv N}$ [31,32].

The morphology of the samples is examined by SEM, as shown in Fig. 1. Fig. 1**a** shows that the NiFe-PBAs precursor has the morphology of nanocubes with a smooth surface and side length of ~150 nm distributed uniformly on CC. After the thermal treatment at 200–300 °C, the nanocube morphology is maintained well as revealed in Fig. 1**b-d**. When the thermal temperature is 300 °C, the surface of the nanocubes became rough and porous as shown in Fig. 1**d**. The porous structure is formed by the escape of C≡N species from NiFe-PBAs at high temperatures. The TEM image in Fig. S1a shows the porous structure of the nanocube, confirming the result indicated in the SEM. The HR-TEM in Fig. S1b implies the lattice space of 0.23 nm, which can be ascribed to the (420) planes of $KNiFe(CN)_6$.

The Raman scattering spectra in Fig. 2**a** disclose two main peaks at 2160 and 2189 cm^{-1}, corresponding to C≡N vibrations of Fe^{2+}–C≡N–Ni^{2+} and Fe^{3+}–C≡N–Ni^{2+}, respectively [33]. The peak at 2189 cm^{-1} weakens with increasing temperature compared to the NiFe-PBAs precursor, indicating a decrease of C≡N and generation of $V_{C\equiv N}$ in NiFe-PBAs. The peaks at 2160 and 2189 cm^{-1} of PBAs-300 almost disappear suggesting the $V_{C\equiv N}$ is generated in Fe^{3+}–C≡N–Ni^{2+} and Fe^{2+}–C≡N–Ni^{2+} at a higher temperature, thus confirming the generation of $V_{C\equiv N}$ after the thermal treatment. Fig. 2**b** shows that the diffraction peaks can be indexed to $KNiFe(CN)_6$ (JCPDS card No. 51–1897). The diffraction peaks decrease with increasing temperature possibly because of structural distortion arising from the generation of $V_{C\equiv N}$ [34].

The chemical composition and chemical states are determined by XPS. Fig. S2 discloses the presence of C, N, Ni, and Fe. The peaks at 874.1, 876.1, and 880.7 eV in Fig. 3**a** can be ascribed to Ni(II), Ni(III), and the satellite peak of Ni $2p_{1/2}$, respectively, which agree well with the previous literature [35,36]. Fig. 3**b** shows the peaks at 721.5, 724.0, and 725.0 eV originate from Fe-C, Fe(II), and Fe(III) of Fe $2p_{1/2}$, respectively, similar to the reported literature [37–40]. As the processing temperature goes up, the surface Ni(III) concentration decreases but the Fe(III) concentration increases as shown in Fig. 3**c**. The results reveal electronic interactions between the Ni and Fe atoms after the thermal treatment and electrons are transferred from Fe to Ni atoms, in agreement with findings by Yu et al. [21]. The Fe sites with higher oxidation states have a stronger ability to adsorb OH^- and consequently facilitate the formation of the FeOOH active layer which plays a key role in enhancing the OER properties [41].

The elemental composition is determined by XPS as shown in Table S1. The ratio of Ni:Fe is consistent at the surface. The N *1s* peak at 398.4 eV originates from C≡N (Fig. S3). The N:Ni and Fe-C:Fe(III) ratios (Table S1 and Fig. 3**d**) decrease with increasing temperature, indicating a deficiency of N atoms at the surface due to the formation of $V_{C\equiv N}$ [32]. According to the changes in the N:Ni ratios with temperature, the amounts of $V_{C\equiv N}$ have been calculated as shown in Fig. 3**e**. The $V_{C\equiv N}$ concentration increases with increasing temperature and nearly 80% C≡N deficiency is observed on the surface after heating at 300 °C. The precisely regulated $V_{C\equiv N}$ in the PBAs-based electrocatalyst plays an important role in the enhanced catalytic activity as well as reaction kinetics [21].

3.2. Electrocatalytic OER performance

The electrochemical properties of the electrocatalysts are determined using a three-electrode system in 1 M KOH. Fig. 4**a** shows that the C≡N deficient electrocatalysts have smaller overpotentials than the NiFe-PBAs precursor, suggesting that $V_{C\equiv N}$ enhance the OER activity. In particular, PBAs-250 has excellent OER characteristics such as an overpotential of only 270 mV for a large current density of 50 mA cm^{-2}, which is smaller than those of PBAs-200 (342 mV) and PBAs-300 (312 mV). The improvement of PBAs-250 compared to PBAs-200 can be attributed to more $V_{C\equiv N}$ which modifies the electronic configuration and facilitates surface reconstruction of Fe active sites. However, the inferior performance of PBAs-300 with excess $V_{C\equiv N}$ compared to PBAs-250 may stem from structural damage and electron transfer impediment

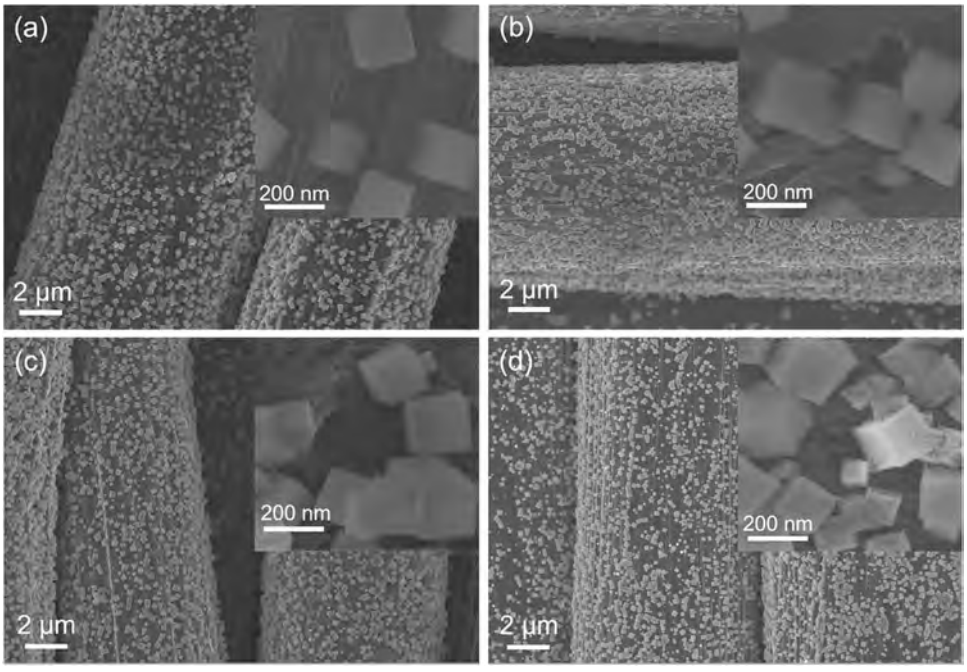

Fig. 1. SEM images of (a) NiFe-PBAs, (b) PBAs-200, (c) PBAs-250, and (d) PBAs-300.

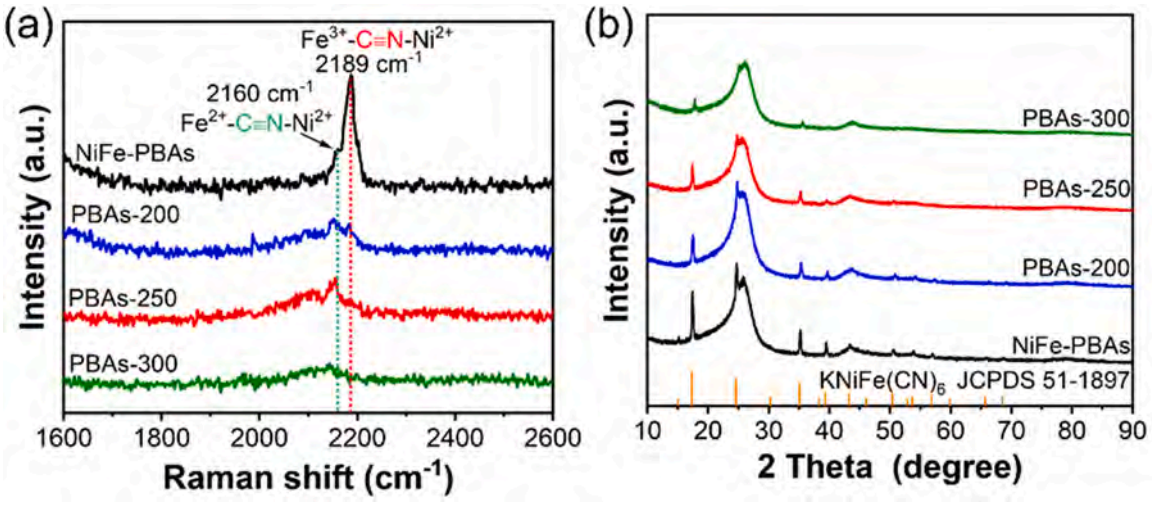

Fig. 2. (a) Raman scattering and (b) XRD of NiFe-PBAs, PBAs-200, PBAs-250, and PBAs-300.

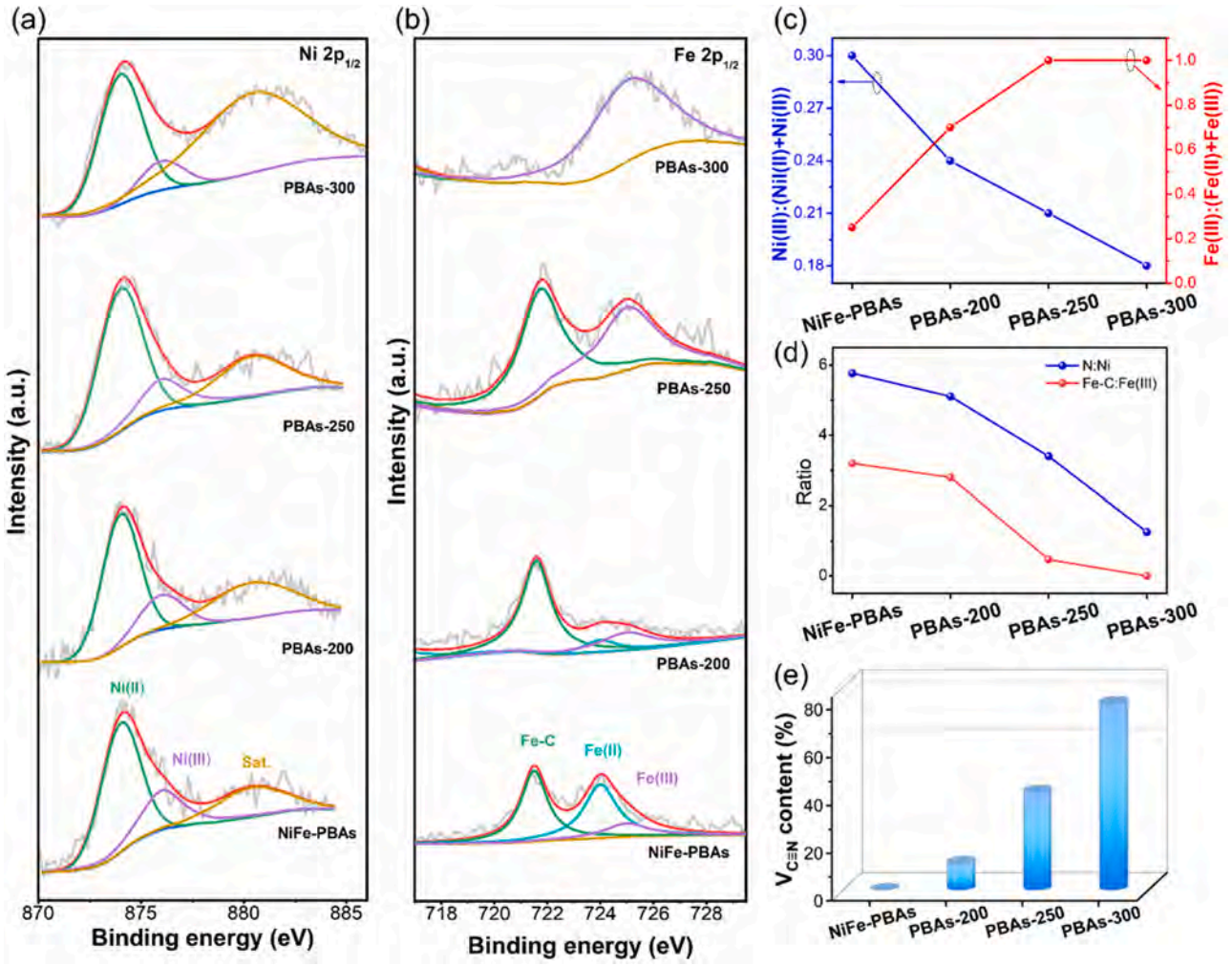

Fig. 3. High-resolution XPS spectra of (a) Ni $2p_{1/2}$ and (b) Fe $2p_{1/2}$, (c) Ni(III) and Fe(III) contents, (d) Ratios of N:Ni and Fe-C:Fe(III), and (e) $V_{C\equiv N}$ contents in NiFe-PBAs, PBAs-200, PBAs-250, and PBAs-300.

caused by too many vacancies and defects [28].

Fig. 4**b** shows that the Tafel slopes of the C≡N deficient PBAs electrocatalysts are smaller than that of the NiFe-PBAs precursor, indicating that the introduction of $V_{C\equiv N}$ into PBAs improves the OER kinetics. The Tafel slope of PBAs-250 is 53 mV dec^{-1} and less than those of PBAs-200 (74 mV dec^{-1}) and PBAs-300 (64 mV dec^{-1}), implying faster reaction kinetics and lower charge and mass transport barriers in OER if the amount of $V_{C\equiv N}$ is moderate (PBAs-250). However, too many $V_{C\equiv N}$

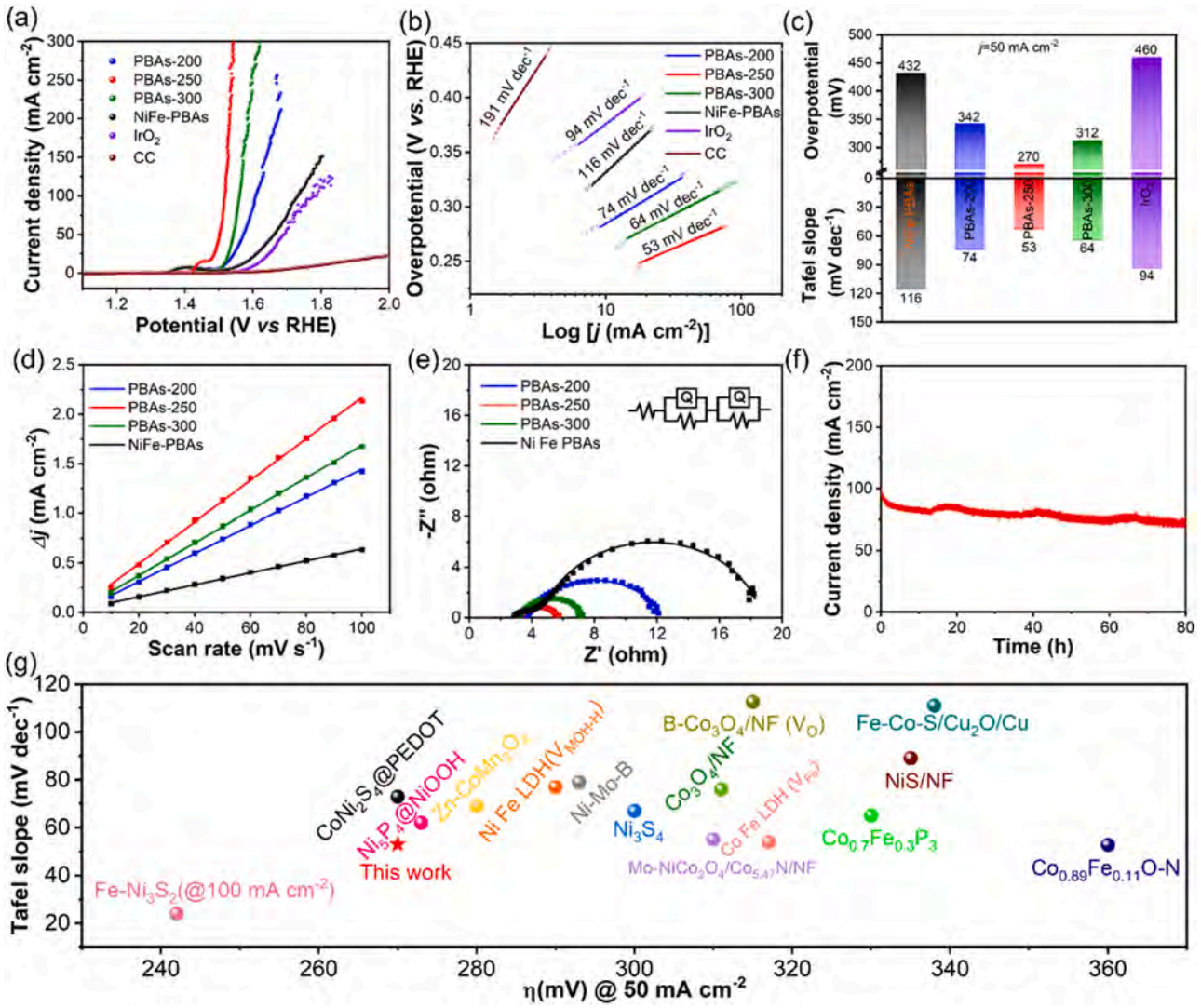

Fig. 4. Electrochemical characteristics of the electrocatalysts: (a) Polarization curves, (b) Tafel plots (c) Comparison of the overpotentials required at 50 mA cm^{-2} and Tafel slopes, (d) ECSA, (e) EIS, (f) Stability test of PBAs-250 in 1 M KOH, and (g) Comparison of the overpotentials required at 50 mA cm^{-2} and Tafel slopes with those of previously reported OER catalysts.

retard the OER kinetics possibly due to electron trapping by C≡N defects. Fig. 4**c** compares the overpotentials required at 50 mA cm^{-2} and Tafel slopes of different electrocatalysts corroborating the excellent properties of PBAs-250 in OER.

The electrochemical active surface area (ESCA) is derived based on the electrochemical double-layer capacitance (C_{dl}), as shown in Figs. S4 and 4**d**. PBAs-250 has the highest C_{dl} of 20.9 mF cm^{-2} compared to NiFe-PBAs (6.1 mF cm^{-2}), PBAs-200 (14.1 mF cm^{-2}), and PBAs-300 (16.4 mF cm^{-2}). Generally, the larger the ECSA, the more exposed active sites and the higher the electrocatalytic activity. The large ECSA of PBAs-250 stems from the synergistic effect of $V_{C\equiv N}$ and Ni-Fe electronic interactions. The charge transfer resistance (R_{ct}) during OER is determined by electrochemical impedance spectroscopy (EIS), as shown in Fig. 4**e**. PBAs-250 has the smallest R_{ct} of 2.7 Ω compared to NiFe-PBAs (15.2 Ω), PBAs-200 (9.1 Ω), and PBAs-300 (4.2 Ω). The results reveal fast charge and mass transfer with a moderate amount of $V_{C\equiv N}$.

Stability is an important parameter in practice and chronoamperometry is performed for more than 80 h. Fig. 4**f** indicates that the PBAs-250 electrocatalyst has outstanding stability. Formation of $V_{C\equiv N}$ generates a large number of unsaturated Fe sites around the vacancies and the unsaturated Fe sites are more likely to reconstruct and form the FeOOH active layer during OER rather than being etched by OH^-, thereby giving rise to the excellent stability [42,43]. Fig. 4**g** illustrated the comparison of the overpotentials required at 50 mA cm^{-2} and Tafel slopes with those of previously reported OER catalysts including NiFe LDH [44], Ni-Mo-B [45], Ni_3S_4 [46], Co_3O_4/NF [47], B-Co_3O_4/NF [48], Mo-$NiCo_2O_4$/$Co_{5.47}$N/NF [49], CoFe LDH [50], $Co_{0.7}Fe_{0.3}P_3$ [51], NiS/NF [52], Fe-Co-S/Cu_2O/Cu [53], $Co_{0.89}Fe_{0.11}$O-N [54], $CoNi_2S_4$ @PEDOE [55], Ni_5P_4 @NiOOH [56], Fe-Ni_3S_2 [57], and Zn-$CoMn_2O_4$ [58]. The morphology and composition of PBAs-250 before and after the durability test are investigated. Fig. 5**a** shows that the crystal structure of PBAs-250 remains the same after the long-term test, which still can be indexed to $KNiFe(CN)_6$ (JCPDS card No. 51–1897). Fig. 5**b** shows that the nanocube morphology remains although the surface becomes rough due to the surface reconstruction during OER [59]. Fig. 5**c** indicates the disappearance of the Fe-C signal compared to the fresh sample (Fig. 3**b**), suggesting the conversion from Fe-C into Fe^{3+} after long-term OER on account of surface reconstruction and formation of FeOOH [8,10].

The Faradaic efficiency of PBAs-250 in OER is determined by the water displacement method as illustrated in Fig. 6**a**. 43.5 mL of O_2 are generated in 120 min at a current of 100 mA (Fig. 6**b**) and the Faradaic efficiency is calculated to be 95.4% which is close to 100%. It can thus be concluded that the NiFe-PBAs-based electrocatalyst with the

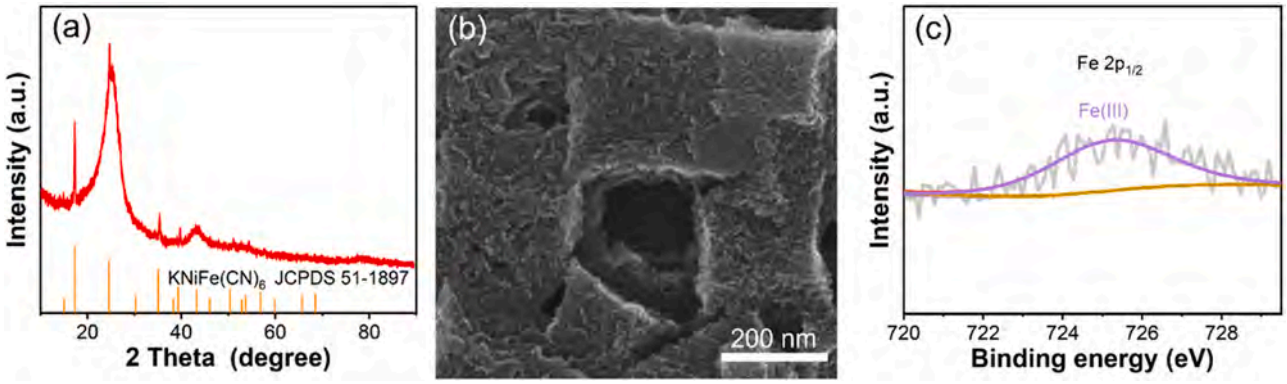

Fig. 5. (a) XRD, (b) SEM image, and (c) Fe $2p_{1/2}$ XPS spectrum of PBAs-250 after the long-term test.

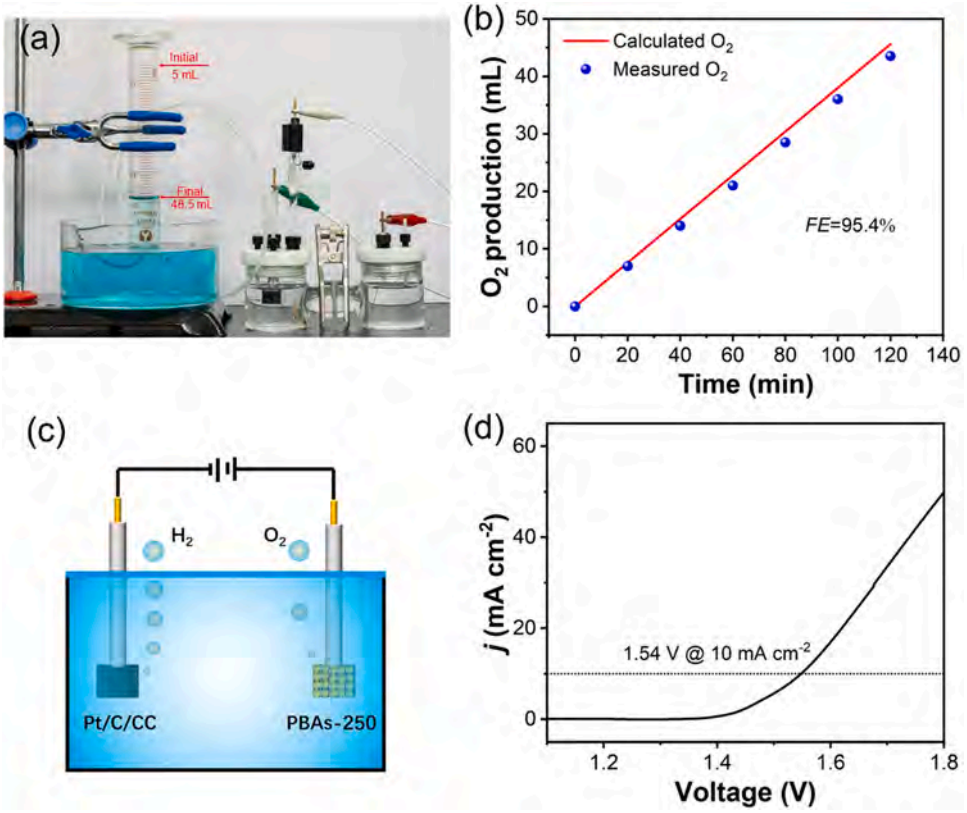

Fig. 6. (a) Photograph of the OER system consisting of the PBAs-250 electrocatalyst with O_2 gas generation determined by the water displacement method, (b) Experimental and theoretical amounts of O_2 produced by the PBAs-250 electrocatalyst at a current of 100 mA in 1 M KOH, (c) Schematic showing the overall reaction in the apparatus consisting of the Pt/C/CC cathode and PBAs-250 anode, and (d) Polarization curve of the overall reaction.

appropriate amount of $V_{C\equiv N}$ is an excellent OER electrocatalyst. To further explore the overall water-splitting performance of the PBAs-250 electrocatalyst, a two-electrode system composed of the commercial Pt/C modified CC electrode (Pt/C/CC) as the cathode and PBAs-250 as the anode is assembled, as schematically illustrated in Fig. 6**c**. Fig. 6**d** shows that the cell requires a low voltage of 1.54 V for a current density of 10 mA cm^{-2}, which is smaller than those of similar Ni-based electrocatalysts listed in Table S3.

3.3. Extend to other PBAs

The concept of $V_{C\equiv N}$ introduction and regulation can be extended to other PBAs-based materials. NiCo-PBAs nanocubes are prepared by the same protocol and the nanocube morphology is maintained after the thermal treatment as shown in Fig. S5. Fig. 7**a** shows the crystal structure of the NiCo-PBAs precursor and thermally treated electrocatalyst (NiCo-PBAs-V), both can be indexed to $Ni_3[Co(CN)_6]_2$ (JCPDS Card No. 89–3738). After the thermal treatment, $V_{C\equiv N}$ is formed as revealed by the Raman scattering spectra in Fig. 7**b**, which shows weakened C≡N vibration peaks at 2190 and 2208 cm^{-1} [60]. The C≡N deficient NiCo-PBAs-V electrocatalyst shows a smaller overpotential and Tafel slope than the NiCo-PBAs precursor, as shown in Fig. 7**c, d**. Figs. S6 and 7**e** disclose that the ECSA of the C≡N deficient NiCo-PBAs-V is enlarged by 16% compared to the precursor because of the $V_{C\equiv N}$ and activation of active sites. The smaller R_{ct} disclosed by EIS in Fig. 7**f** of the NiCo-PBAs-V confirms the fast reaction kinetics.

4. Conclusions

A precise regulating strategy to tune the $V_{C\equiv N}$ content in NiFe- and

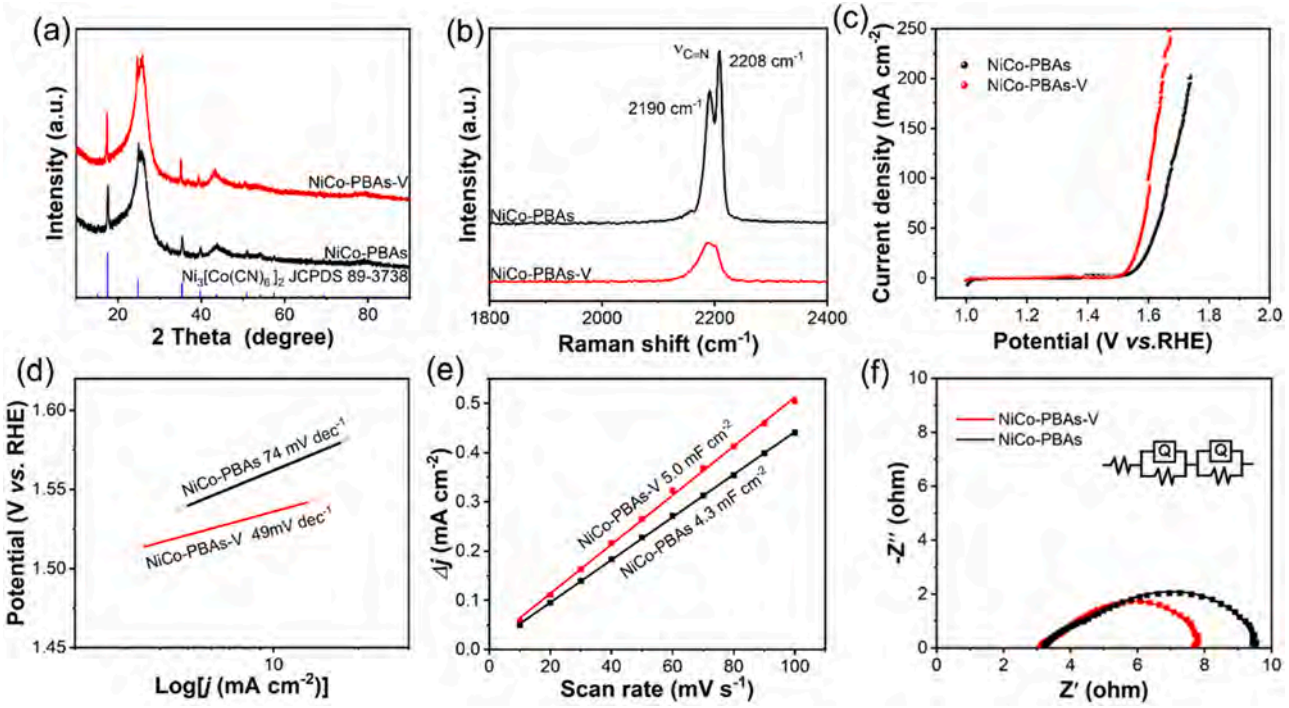

Fig. 7. (a) XRD patterns, (b) Raman scattering spectra, (c) Polarization curves, (d) Tafel plots, (e) ECSA, and (f) EIS of NiCo-PBAs and NiCo-PBAs-V.

NiCo-PBAs for enhanced OER is described. The amount of $V_{C\equiv N}$ can be tuned precisely by the thermal treatment of the electrocatalysts. $V_{C\equiv N}$ not only modulates the local electronic structure of the metal sites but also creates unsaturated Fe sites to facilitate the formation of a catalytically active phase. The electronic interactions between Ni and Fe sites further optimize the electronic structure of the active sites for OER. Furthermore, the $V_{C\equiv N}$ restrains the etching of the catalyst during OER to present outstanding long-term stability. As a result, the $V_{C\equiv N}$ modified NiFe-PBAs electrocatalyst has excellent OER characteristics such as a low overpotential of 270 mV at 50 mA cm^{-2} and outstanding stability for 80 h in an alkaline solution. The $V_{C\equiv N}$ deficient NiFe-PBAs also shows a small voltage of 1.54 V at 10 mA cm^{-2} in overall water splitting with the commercial Pt/C catalyst as the cathode in 1 M KOH electrolyte. The results suggest that improved energy conversion efficiency has been achieved by precisely regulating the $V_{C\equiv N}$ deficient in NiFe-PBAs. Our work provides insights into the modification of PBAs for advanced OER and energy-efficient hydrogen production.

CRediT authorship contribution statement

Wenhao Deng: Methodology, Investigation, Writing – original draft preparation. **Baochai Xu:** Methodology, Investigation, Writing – original draft preparation, **Qiangqiang Zhao:** Methodology, Investigation, **Song Xie:** Methodology, Investigation, **Weihong Jin:** Investigation, Writing – original draft preparation, **Xuming Zhang:** Investigation, Writing – original draft preparation, **Biao Gao:** Investigation, Writing – original draft preparation, **Zhitian Liu:** Conceptualization, Writing – review & editing, **Zaenab Abd-Allah:** Writing – review & editing, **Paul K Chu:** Writing – review & editing, **Xiang Peng:** Supervision, Conceptualization, Writing – original draft preparation, Writing – review & editing, Funding acquisition. All authors discussed the results and commended the manuscript.

Declaration of Competing Interest

The authors declare that they have no known competing financial interests or personal relationships that could have appeared to influence the work reported in this paper.

Data availability

Data will be made available on request.

Acknowledgments

This work was financially supported by the Key Research and Development Program of Hubei Province (2021BAA208), National Natural Science Foundation of China (52002294), Knowledge Innovation Program of Wuhan-Shuguang Project (2022010801020364), City University of Hong Kong Donation Research Grant (DON-RMG 9229021), City University of Hong Kong Donation Grant (9220061), and City University of Hong Kong Strategic Research Grant (SRG) (7005505).

Appendix A. Supporting information

Supplementary data associated with this article can be found in the online version at doi:10.1016/j.jece.2023.109407.

References

[1] H. Ding, H. Liu, W. Chu, C. Wu, Y. Xie, Structural transformation of heterogeneous materials for electrocatalytic oxygen evolution reaction, Chem. Rev. 121 (2021) 13174–13212.
[2] X. Peng, Y. Yan, X. Jin, C. Huang, W. Jin, B. Gao, P.K. Chu, Recent advance and prospectives of electrocatalysts based on transition metal selenides for efficient water splitting, Nano Energy 78 (2020), 105234.
[3] L. Xiong, Y. Qiu, X. Peng, Z. Liu, P.K. Chu, Electronic structural engineering of transition metal-based electrocatalysts for the hydrogen evolution reaction, Nano Energy 104 (2022), 107882.
[4] J. Wang, S.-J. Kim, J. Liu, Y. Gao, S. Choi, J. Han, H. Shin, S. Jo, J. Kim, F. Ciucci, H. Kim, Q. Li, W. Yang, X. Long, S. Yang, S.-P. Cho, K.H. Chae, M.G. Kim, H. Kim, J. Lim, Redirecting dynamic surface restructuring of a layered transition metal oxide catalyst for superior water oxidation, Nat. Catal. 4 (2021) 212–222.
[5] S. Anantharaj, S. Noda, V.R. Jothi, S. Yi, M. Driess, P.W. Menezes, Strategies and perspectives to catch the missing pieces in energy-efficient hydrogen evolution reaction in alkaline media, Angew. Chem. Int. Ed. 60 (2021) 18981–19006.
[6] X. Peng, X. Jin, B. Gao, Z. Liu, P.K. Chu, Strategies to improve cobalt-based electrocatalysts for electrochemical water splitting, J. Catal. 398 (2021) 54–66.

[7] D. Zhou, P. Li, X. Lin, A. McKinley, Y. Kuang, W. Liu, W.-F. Lin, X. Sun, X. Duan, Layered double hydroxide-based electrocatalysts for the oxygen evolution reaction: Identification and tailoring of active sites, and superaerophobic nanoarray electrode assembly, Chem. Soc. Rev. 50 (2021) 8790–8817.

[8] X. Peng, X. Jin, N. Liu, P. Wang, Z. Liu, B. Gao, L. Hu, P.K. Chu, A high-performance electrocatalyst composed of nickel clusters encapsulated with a carbon network on TiN nanaowire arrays for the oxygen evolution reaction, Appl. Surf. Sci. 567 (2021), 150779.

[9] J. Tang, J. Xu, Z. Ye, X. Li, J. Luo, Microwave sintered porous CoCrFeNiMo high entropy alloy as an efficient electrocatalyst for alkaline oxygen evolution reaction, J. Mater. Sci. Technol. 79 (2021) 171–177.

[10] X. Peng, S. Xie, X. Wang, C. Pi, Z. Liu, B. Gao, L. Hu, W. Xiao, P.K. Chu, Energy-saving hydrogen production by methanol oxidation reaction coupled hydrogen evolution reaction co-catalyzed by phase separation induced heterostructure, J. Mater. Chem. A 10 (2022) 20761–20769.

[11] X. Peng, Y. Yan, S. Xiong, Y. Miao, J. Wen, Z. Liu, B. Gao, L. Hu, P.K. Chu, Se-$NiSe_2$ hybrid nanosheet arrays with self-regulated elemental Se for efficient alkaline water splitting, J. Mater. Sci. Technol. 118 (2022) 136–143.

[12] S. Xie, Y. Yan, S. Lai, J. He, Z. Liu, B. Gao, M. Javanbakht, X. Peng, P.K. Chu, Ni^{3+}-enriched nickel-based electrocatalysts for superior electrocatalytic water oxidation, Appl. Surf. Sci. 605 (2022), 154743.

[13] Y. Li, L. Hu, W. Zheng, X. Peng, M. Liu, P.K. Chu, L.Y.S. Lee, Ni/Co-based nanosheet arrays for efficient oxygen evolution reaction, Nano Energy 52 (2018) 360–368.

[14] A. Qayum, X. Peng, J. Yuan, Y. Qu, J. Zhou, Z. Huang, H. Xia, Z. Liu, D.Q. Tan, P. K. Chu, F. Lu, L. Hu, Highly durable and efficient Ni-FeO_x/$FeNi_3$ electrocatalysts synthesized by a facile in situ combustion-based method for overall water splitting with large current densities, ACS Appl. Mater. Interfaces 14 (2022) 27842–27853.

[15] M.B. Zakaria, T. Chikyow, Recent advances in Prussian blue and Prussian blue analogues: Synthesis and thermal treatments, Coord. Chem. Rev. 352 (2017) 328–345.

[16] L.M. Cao, D. Lu, D.C. Zhong, T.B. Lu, Prussian blue analogues and their derived nanomaterials for electrocatalytic water splitting, Coord. Chem. Rev. 407 (2020), 213156.

[17] J. Nai, J. Zhang, X.W. Lou, Construction of single-crystalline Prussian blue analog hollow nanostructures with tailorable topologies, Chem 4 (2018) 1967–1982.

[18] J. Lu, C. Chen, M. Qian, P. Xiao, P. Ge, C. Shen, X.-L. Wu, J. Chen, Hollow-structured amorphous prussian blue decorated on graphitic carbon nitride for photo-assisted activation of peroxymonosulfate, J. Colloid Interf. Sci. 603 (2021) 856–863.

[19] X. Peng, S. Feng, S. Lai, Z. Liu, J. Gao, M. Javanbakht, B. Gao, Structural engineering of rare-earth-based perovskite electrocatalysts for advanced oxygen evolution reaction, Int. J. Hydrogen Energy 47 (2022) 39470–39485.

[20] Z.P. Wu, H. Zhang, S. Zuo, Y. Wang, S.L. Zhang, J. Zhang, S.Q. Zang, X.W. Lou, Manipulating the local coordination and electronic structures for efficient electrocatalytic oxygen evolution, Adv. Mater. 33 (2021), 2103004.

[21] Z.-Y. Yu, Y. Duan, J.D. Liu, Y. Chen, X.K. Liu, W. Liu, T. Ma, Y. Li, X.S. Zheng, T. Yao, Unconventional CN vacancies suppress iron-leaching in Prussian blue analogue pre-catalyst for boosted oxygen evolution catalysis, Nat. Commun. 10 (2019) 2799.

[22] Y. Kang, S. Wang, K.S. Hui, H.F. Li, F. Liang, X.L. Wu, Q. Zhang, W. Zhou, L. Chen, F. Chen, K.N. Hui, $[Fe(CN)_6]$ vacancy-boosting oxygen evolution activity of Co-based Prussian blue analogues for hybrid sodium-air battery, Mater. Today Energy 20 (2021), 100572.

[23] S. Liu, D. Liu, Y. Sun, P. Xiao, H. Lin, J. Chen, X.-L. Wu, X. Duan, S. Wang, Enzyme-mimicking single-atom FeN_4 sites for enhanced photo-Fenton-like reactions, Appl. Catal. B-Environ. 310 (2022), 121327.

[24] X. Wang, Y. Zhang, H. Si, Q. Zhang, J. Wu, L. Gao, X. Wei, Y. Sun, Q. Liao, Z. Zhang, K. Ammarah, L. Gu, Z. Kang, Y. Zhang, Single-atom vacancy defect to trigger high-efficiency hydrogen evolution of MoS_2, J. Am. Chem. Soc. 142 (2020) 4298–4308.

[25] F. Chen, X.-L. Wu, C. Shi, H. Lin, J. Chen, Y. Shi, S. Wang, X. Duan, Molecular engineering toward pyrrolic N-rich M-N_4 (M = Cr, Mn, Fe, Co, Cu) single-atom sites for enhanced heterogeneous fenton-like reaction, Adv. Funct. Mater. 31 (2021), 2007877.

[26] L. Zhang, C. Lu, F. Ye, R. Pang, Y. Liu, Z. Wu, Z. Shao, Z. Sun, L. Hu, Selenic acid etching assisted vacancy engineering for designing highly active electrocatalysts toward the oxygen evolution reaction, Adv. Mater. 33 (2021), 2007523.

[27] X. Yang, Y. Luo, J. Li, H. Wang, Y. Song, J. Li, Z. Guo, Tuning mixed electronic/ionic conductivity of 2D $CdPS_3$ nanosheets as an anode material by synergistic intercalation and vacancy engineering, Adv. Funct. Mater. 32 (2022), 2112169.

[28] C. Lai, H. Li, Y. Sheng, M. Zhou, W. Wang, M. Gong, K. Wang, K. Jiang, 3D Spatial combination of CN vacancy-mediated NiFe-PBA with N-doped carbon nanofibers network toward free-standing bifunctional electrode for Zn-air batteries, Adv. Sci. 9 (2022), 2105925.

[29] L. Han, X.Y. Yu, X.W. Lou, Formation of Prussian-blue-analog nanocages via a direct etching method and their conversion into Ni-Co-mixed oxide for enhanced oxygen evolution, Adv. Mater. 28 (2016) 4601–4605.

[30] J. Nai, B.Y. Guan, L. Yu, X.W. Lou, Oriented assembly of anisotropic nanoparticles into frame-like superstructures, Sci. Adv. 3 (2017), e1700732.

[31] Q. Hu, X. Huang, Z. Wang, G. Li, Z. Han, H. Yang, P. Liao, X. Ren, Q. Zhang, J. Liu, C. He, Slower removing ligands of metal organic frameworks enables higher electrocatalytic performance of derived nanomaterials, Small 16 (2020), 2002210.

[32] H. Yang, J. Liu, Z. Chen, R. Wang, B. Fei, H. Liu, Y. Guo, R. Wu, Unconventional bi-vacancies activating inert Prussian blue analogues nanocubes for efficient hydrogen evolution, Chem. Eng. J. 420 (2021), 127671.

[33] M. Jiang, X. Fan, S. Cao, Z. Wang, Z. Yang, W. Zhang, Thermally activated carbon–nitrogen vacancies in double-shelled NiFe Prussian blue analogue nanocages for enhanced electrocatalytic oxygen evolution, J. Mater. Chem. A 9 (2021) 12734–12745.

[34] S. Wheeler, I. Capone, S. Day, C. Tang, M. Pasta, Low-potential Prussian blue analogues for sodium-ion batteries: Manganese hexacyanochromate, Chem. Mater. 31 (2019) 2619–2626.

[35] S. Chandra Reddy Niragatti, S. Thupakula Venkata Madhukar, J. Kim, K. Yoo, In-situ-grown Co-doped Ni-hexacyanoferrate/Ni-foam composites as battery-type electrode materials for aqueous hybrid supercapacitors, J. Alloy. Compd. 918 (2022), 165638.

[36] Y.Y. Tong, C.D. Gu, J.L. Zhang, H. Tang, Y. Li, X.L. Wang, J.P. Tu, Urchin-like Ni-Co-P-O nanocomposite as novel methanol electro-oxidation materials in alkaline environment, Electrochim. Acta 187 (2016) 11–19.

[37] S. Wu, H. Liu, G. Lei, H. He, J. Wu, G. Zhang, F. Zhang, W. Peng, X. Fan, Y. Li, Single-atomic iron-nitrogen 2D MOF-originated hierarchically porous carbon catalysts for enhanced oxygen reduction reaction, Chem. Eng. J. 441 (2022), 135849.

[38] L. Guo, J. Li, Y. Zeng, R. Kosol, Y. Cui, N. Kodama, X. Guo, R. Prasert, V. Tharapong, G. Liu, J. Wu, G. Yang, Y. Yoneyama, N. Tsubaki, Heteroatom doped iron-based catalysts prepared by urea self-combustion method for efficient CO_2 hydrogenation, Fuel 276 (2020), 118102.

[39] X. Liu, W. Feng, H. Xiang, B. Liu, M. Ye, M. Wei, R. Dong, Y. Chen, K. Dong, Multifunctional cascade nanocatalysts for NIR-II-synergized photonic hyperthermia-strengthened nanocatalytic therapy of epithelial and embryonal tumors, Chem. Eng. J. 411 (2021), 128364.

[40] Y. He, A. del Valle, Y. Qian, Y.-F. Huang, Near infrared light-mediated enhancement of reactive oxygen species generation through electron transfer from graphene oxide to iron hydroxide/oxide, Nanoscale 9 (2017) 1559–1566.

[41] K. Wang, H. Du, S. He, L. Liu, K. Yang, J. Sun, Y. Liu, Z. Du, L. Xie, W. Ai, W. Huang, Kinetically controlled, scalable synthesis of γ-FeOOH nanosheet arrays on nickel foam toward efficient oxygen evolution: The key role of in-situ-generated γ-NiOOH, Adv. Mater. 33 (2021), 2005587.

[42] L. Han, P. Tang, Á. Reyes-Carmona, B. Rodríguez-García, M. Torréns, J.R. Morante, J. Arbiol, J.R. Galan-Mascaros, Enhanced activity and acid pH stability of Prussian blue-type oxygen evolution electrocatalysts processed by chemical etching, J. Am. Chem. Soc. 138 (2016) 16037–16045.

[43] X. Su, Y. Wang, J. Zhou, S. Gu, J. Li, S. Zhang, Operando spectroscopic identification of active sites in NiFe Prussian blue analogues as electrocatalysts: Activation of oxygen atoms for oxygen evolution reaction, J. Am. Chem. Soc. 140 (2018) 11286–11292.

[44] Y. Wu, J. Yang, T. Tu, W. Li, P. Zhang, Y. Zhou, J. Li, J. Li, S. Sun, Evolution of cationic vacancy defects: A motif for surface restructuration of OER precatalyst, Angew. Chem. Int. Ed. 60 (2021) 26829–26836.

[45] H. Liu, X. Li, L. Chen, X. Zhu, P. Dong, M.O.L. Chee, M. Ye, Y. Guo, J. Shen, Monolithic Ni-Mo-B bifunctional electrode for large current water splitting, Adv. Funct. Mater. 32 (2022), 2107308.

[46] K. Wan, J. Luo, C. Zhou, T. Zhang, J. Arbiol, X. Lu, B.-W. Mao, X. Zhang, J. Fransaer, Hierarchical porous Ni_3S_4 with enriched high-valence Ni sites as a robust electrocatalyst for efficient oxygen evolution reaction, Adv. Funct. Mater. 29 (2019), 1900315.

[47] D. Tang, Y. Ma, Y. Liu, K. Wang, Z. Liu, W. Li, J. Li, Amorphous three-dimensional porous Co_3O_4 nanowire network toward superior OER catalysis by lithium-induced, J. Alloy. Compd. 893 (2022), 162287.

[48] H. Yuan, S. Wang, Z. Ma, M. Kundu, B. Tang, J. Li, X. Wang, Oxygen vacancies engineered self-supported B doped Co_3O_4 nanowires as an efficient multifunctional catalyst for electrochemical water splitting and hydrolysis of sodium borohydride, Chem. Eng. J. 404 (2021), 126474.

[49] W. Liu, L. Yu, R. Yin, X. Xu, J. Feng, X. Jiang, D. Zheng, X. Gao, X. Gao, W. Que, P. Ruan, F. Wu, W. Shi, X. Cao, Non-3d metal modulation of a 2D Ni–Co heterostructure array as multifunctional electrocatalyst for portable overall water splitting, Small 16 (2020), 1906775.

[50] Z. Kong, J. Chen, X. Wang, X. Long, X. She, D. Li, D. Yang, Cation vacancy driven efficient CoFe-LDH-based electrocatalysts for water splitting and Zn-air batteries, Mater. Adv. 2 (2021) 7932–7938.

[51] L. Lin, Q. Fu, Y. Han, J. Wang, X. Zhang, Y. Zhang, C. Hu, Z. Liu, Y. Sui, X. Wang, Fe doped skutterudite-type CoP_3 nanoneedles as efficient electrocatalysts for hydrogen and oxygen evolution in alkaline media, J. Alloy. Compd. 808 (2019), 151767.

[52] W. Zhu, X. Yue, W. Zhang, S. Yu, Y. Zhang, J. Wang, J. Wang, Nickel sulfide microsphere film on Ni foam as an efficient bifunctional electrocatalyst for overall water splitting, Chem. Commun. 52 (2016) 1486–1489.

[53] J. Sun, P. Song, H. Zhou, L. Lang, X. Shen, Y. Liu, X. Cheng, X. Fu, G. Zhu, A surface configuration strategy to hierarchical Fe-Co-S/Cu_2O/Cu electrodes for oxygen evolution in water/seawater splitting, Appl. Surf. Sci. 567 (2021), 150757.

[54] Q. Du, P. Su, Z. Cao, J. Yang, C.A.H. Price, J. Liu, Construction of N and Fe co-doped CoO/Co_xN interface for excellent OER performance, Sustain. Mater. Techno. 29 (2021), e00293.

[55] H. Liu, D. Zhao, M. Dai, X. Zhu, F. Qu, A. Umar, X. Wu, PEDOT decorated $CoNi_2S_4$ nanosheets electrode as bifunctional electrocatalyst for enhanced electrocatalysis, Chem. Eng. J. 428 (2022), 131183.

[56] T. Wang, X. Li, Y. Pang, X. Gao, Z. Kou, J. Tang, J. Wang, Unlocking the synergy of interface and oxygen vacancy by core-shell nickel phosphide@oxyhydroxide nanosheets arrays for accelerating alkaline oxygen evolution kinetics, Chem. Eng. J. 425 (2021), 131491.

[57] B. Zhong, B. Cheng, Y. Zhu, R. Ding, P. Kuang, J. Yu, Hierarchically porous nickel foam supported Fe-Ni_3S_2 electrode for high-current-density alkaline water splitting, J. Colloid Interf. Sci. 629 (2023) 846–853.
[58] D. Zhao, R. Zhang, M. Dai, H. Liu, W. Jian, F.Q. Bai, X. Wu, Constructing high efficiency $CoZn_xMn_{2-x}O_4$ electrocatalyst by regulating the electronic structure and surface reconstruction, Small 18 (2022), 2107268.
[59] F. Ma, Q. Wu, M. Liu, L. Zheng, F. Tong, Z. Wang, P. Wang, Y. Liu, H. Cheng, Y. Dai, Z. Zheng, Y. Fan, B. Huang, Surface fluorination engineering of NiFe Prussian blue analogue derivatives for highly efficient oxygen evolution reaction, ACS Appl. Mater. Interfaces 13 (2021) 5142–5152.
[60] S.F. Kettle, E. Diana, E.M. Marchese, E. Boccaleri, P.L. Stanghellini, The vibrational spectra of the cyanide ligand revisited: The ν(CN) infrared and Raman spectroscopy of Prussian blue and its analogues, J. Raman Spectrosc. 42 (2011) 2006–2014.

Supporting Information

C≡N vacancy engineering of Prussian blue analogs for the advanced oxygen evolution reaction

Wenhao Deng[a,#], *Baochai Xu*[a,#], *Qiangqiang Zhao*[a], *Song Xie*[a], *Weihong Jin*[b], *Xuming Zhang*[c], *Biao Gao*[c], *Zhitian Liu*[a], *Zaenab Abd-Allah*[d], *Paul K Chu*[e], *Xiang Peng*[a]*

[a] Hubei Key Laboratory of Plasma Chemistry and Advanced Materials, Hubei Engineering Technology Research Center of Optoelectronic and New Energy Materials, School of Materials Science and Engineering, Wuhan Institute of Technology, Wuhan, 430205, China

[b] Institute of Advanced Wear & Corrosion Resistant and Functional Materials, Jinan University, Guangzhou, 510632, China

[c] State Key Laboratory of Refractories and Metallurgy and Institute of Advanced Materials and Nanotechnology, Wuhan University of Science and Technology, Wuhan, 430081, China

[d] Department of Engineering, Manchester Metropolitan University, John Dalton Building, Manchester M15 6BH, United Kingdom

[e] Department of Physics, Department of Materials Science and Engineering, and Department of Biomedical Engineering, City University of Hong Kong, Tat Chee Avenue, Kowloon, Hong Kong, China

[#] These authors contributed equally to this work.

* Correspondence: xpeng@wit.edu.cn

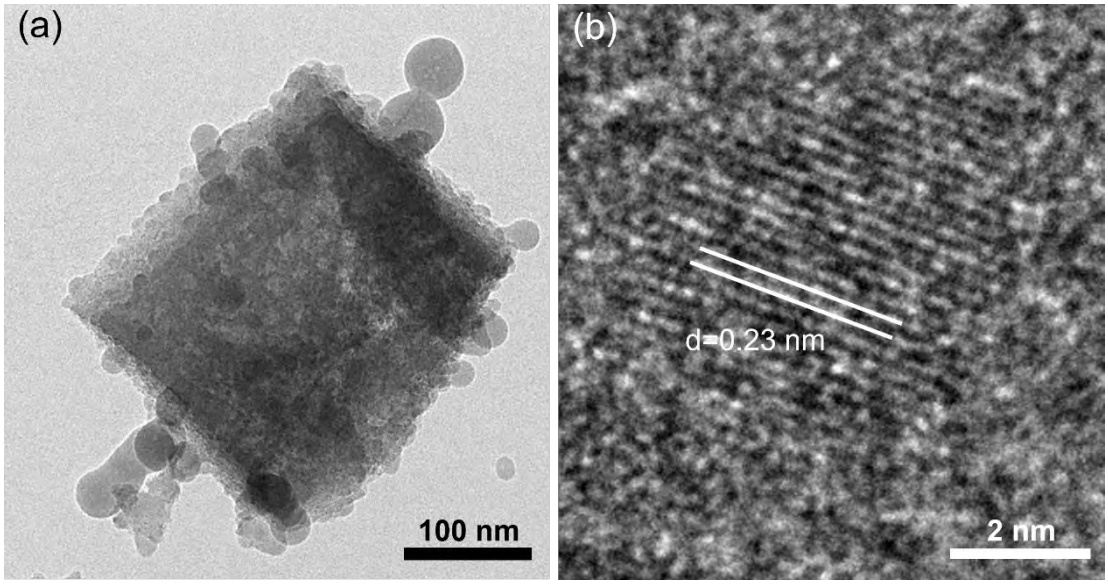

Figure S1. (a) TEM and (b) HR-TEM images of the PBAs-250 electrocatalyst.

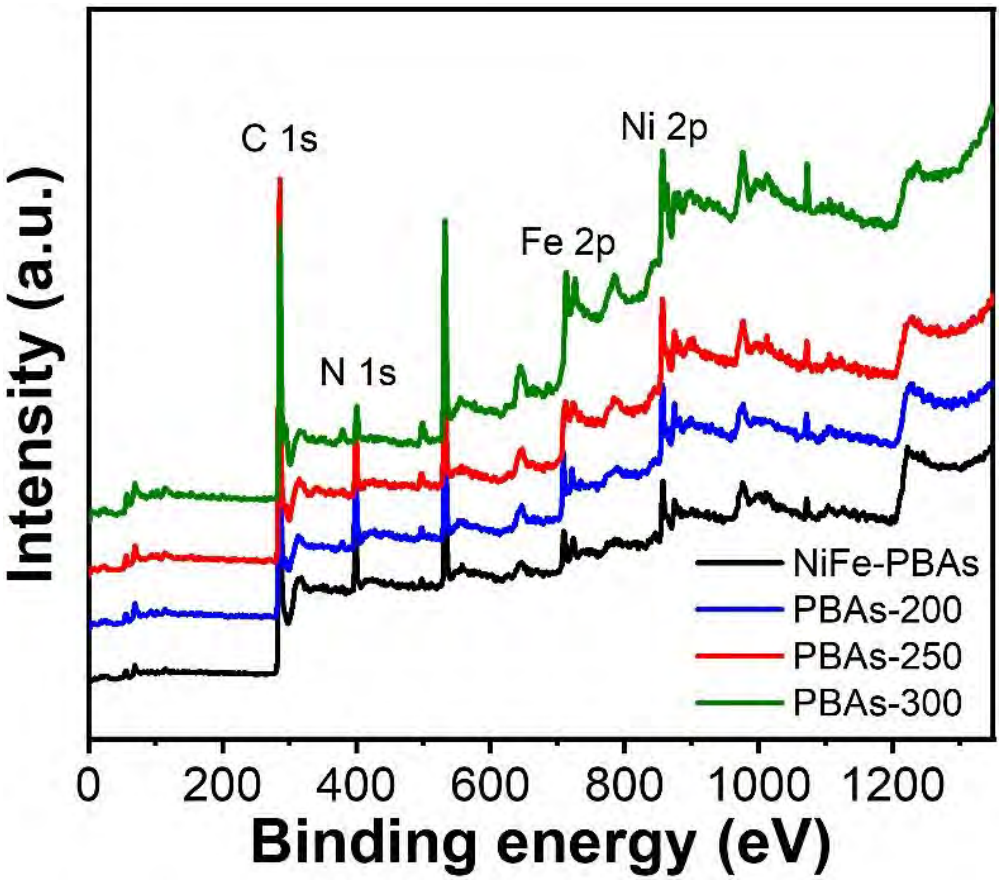

Figure S2. XPS spectra of NiFe-PBAs/CC, PBAs-200, PBAs-250, and PBAs-300.

Table S1. Surface atomic concentrations of the as-prepared electrocatalysts determined by XPS.

Samples	Ratio			
	NiFe-PBAs/CC	**PBAs-200**	**PBAs-250**	**PBAs-300**
Fe:Ni	1.10	1.08	1.08	1.06
N:Ni	5.77	5.11	3.40	1.25
N:Fe	5.25	4.73	3.15	1.18
$V_{C\equiv N}$ content [a]	0%	11.4%	41.1%	78.3%

[a] The $V_{C\equiv N}$ content is determined by the N:Ni ratio.

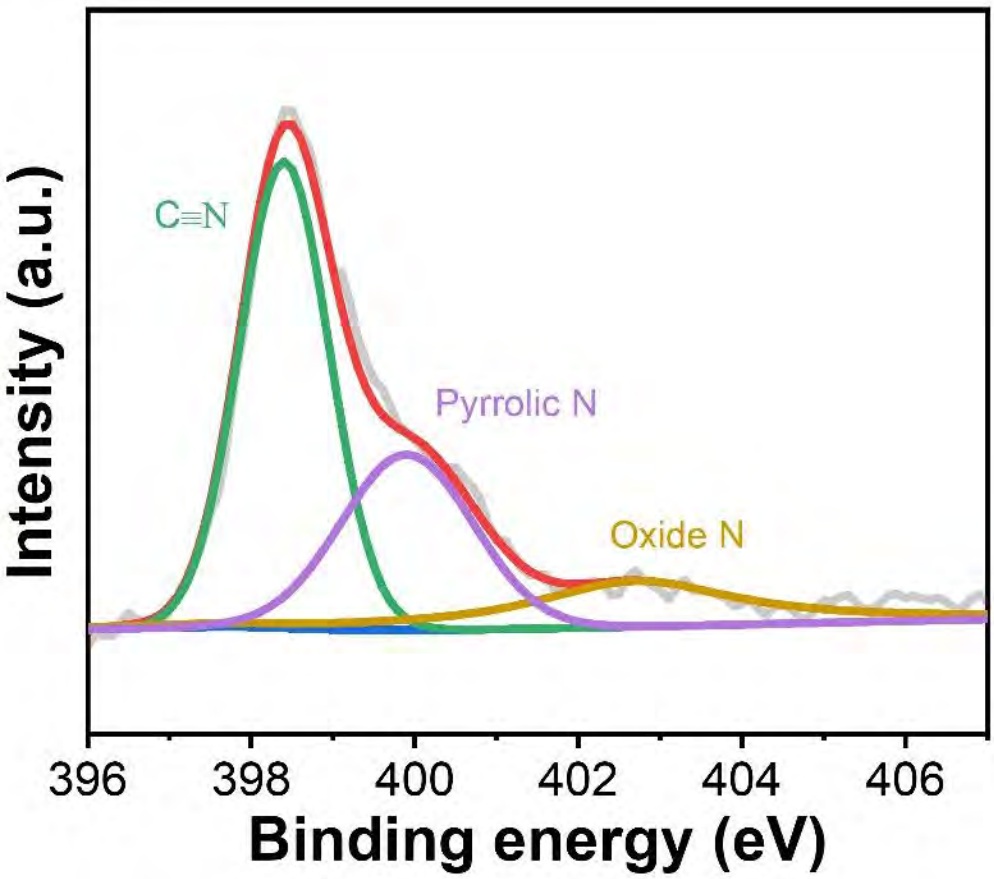

Figure S3. High-resolution N 1*s* XPS spectrum of PBAs-250.

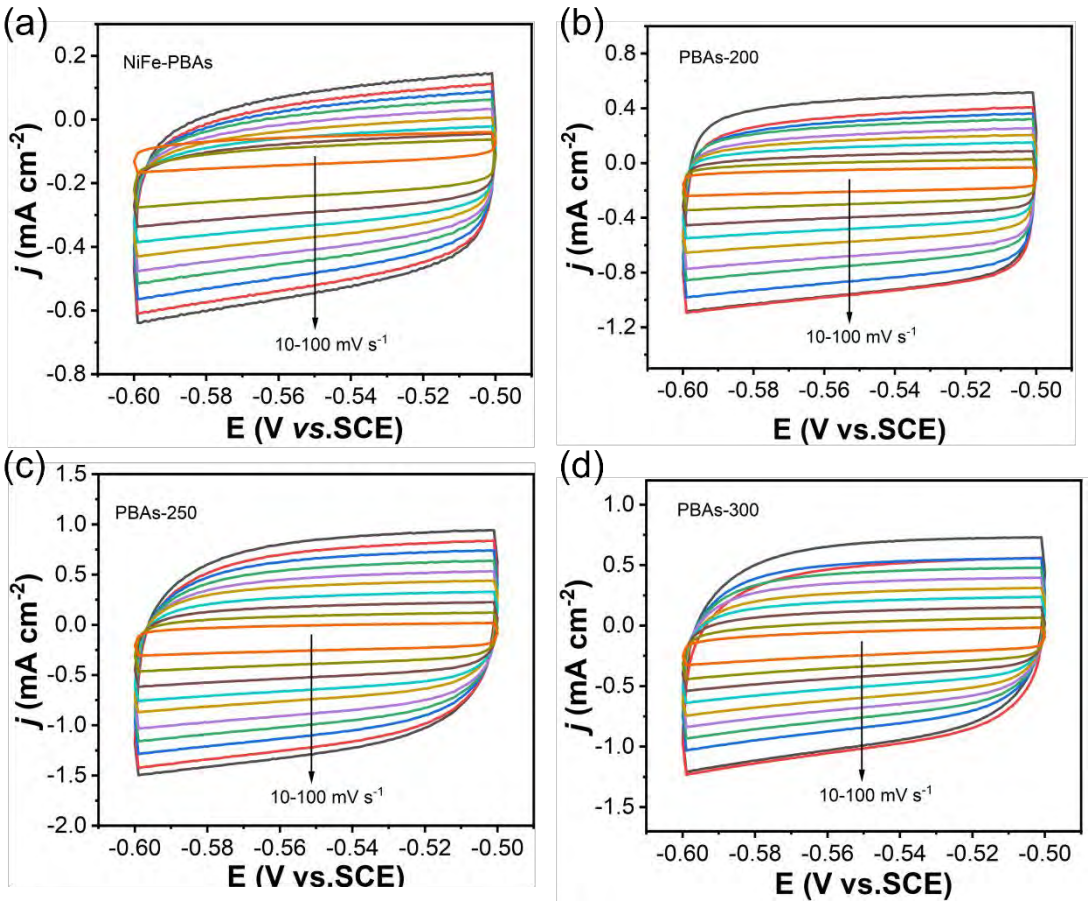

Figure S4. Cyclic voltammograms of (a) NiFe-PBAs/CC, (b) PBAs-200, (c) PBAs-250, and (d) PBAs-300 in the double layer region at scanning rates of 10~100 mV s^{-1} in 1 M KOH.

Table S2. Comparison of the overpotentials at 50 mA cm^{-2} and Tafel slopes of various OER electrocatalysts.

Electrocatalysts	η_{50} [a] [mV]	Tafel slope [mV dec^{-1}]	References
Ni Fe PBAs with CN vacancy	270	53	This work
Ni_3S_4	300	67	[1]
$Co_{0.7}Fe_{0.3}P_3$	330	65.1	[2]
CoFe LDH with Fe vacancy	317	54	[3]
NiS/NF	335	89	[4]
$Co_{0.89}Fe_{0.11}O$-N	360	52.7	[5]
B-Co_3O_4/NF with O vacancy	315	112.5	[6]
Fe-Co-S/Cu_2O/Cu	338	111	[7]
NiFe LDH with (Ni/Fe)OH-H vacancy	290	77	[8]
Mo-$NiCo_2O_4$/$Co_{5.47}N$/NF	310	55.1	[9]
Ni-Mo-B	293	79	[10]
Co_3O_4/NF	311	76	[11]
$CoNi_2S_4$@PEDOT	270	72.9	[12]
Ni_5P_4@NiOOH	273	62	[13]
Zn-$CoMn_2O_4$	280	69.1	[14]
Fe-Ni_3S_2	242@100 mA cm^{-2}	24	[15]

[a] Overpotential at the current density of 50 mA cm^{-2}.

Table S3. Comparison of the voltages required at 10 mA cm^{-2} for overall water splitting in 1 M KOH.

Anodes	Cathode	Voltage [V @ 10 mA cm^{-2}]	References
NiFe-PBAs with CN vacancy	Pt/C	1.54	This work
N-$Ni_2P_4O_{12}$/CC	Pt foil	1.60	[16]
Stainless steel mesh- cathodization	Pt plated electrode	1.59	[17]
NiCoFeB	NiCoFeB	1.75	[18]
Ni/$Ni(OH)_2$	Ni/$Ni(OH)_2$	1.59	[19]
Ni_3N/Co_2N	Ni_3N/Co_2N	1.55	[20]
Ni_3Se_2/$MoSe_x$	Ni_3Se_2/MoSex	1.57	[21]

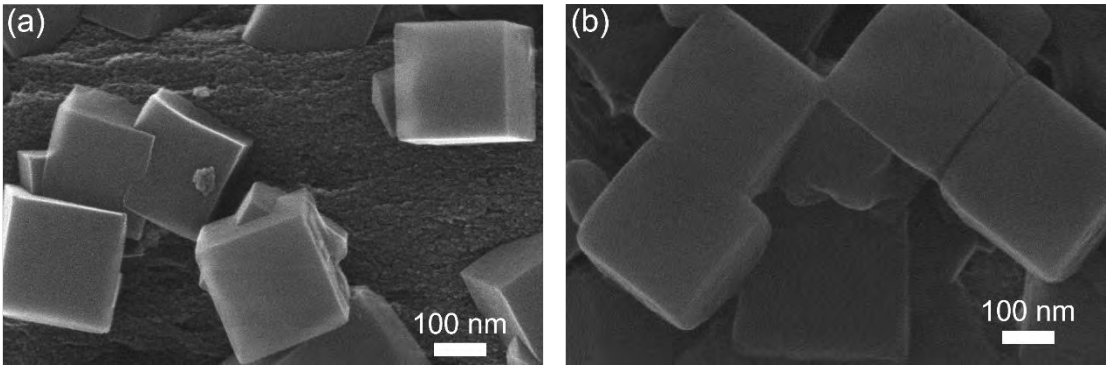

Figure S5. SEM images of (a) NiCo-PBAs and (b) NiCo-PBAs-V.

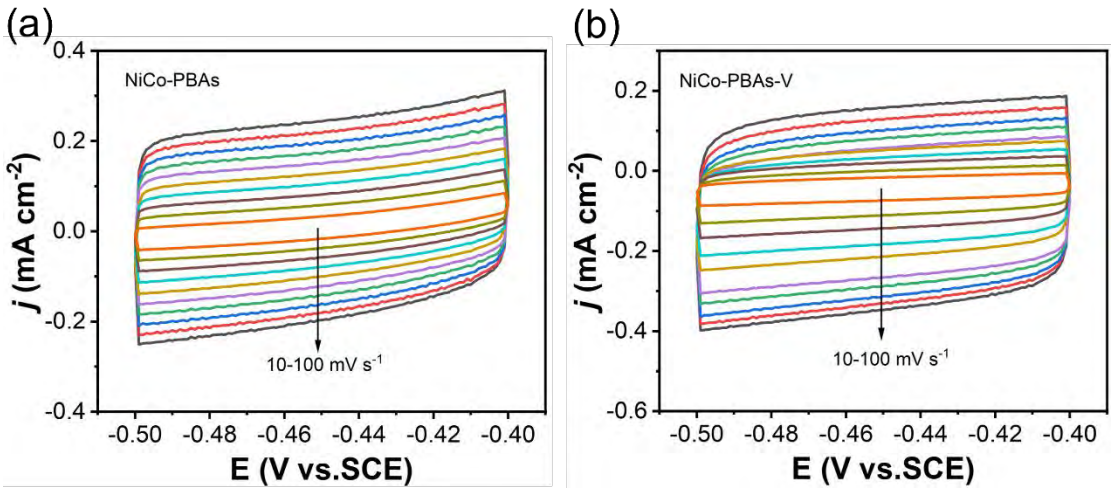

Figure S6. Cyclic voltammograms of (a) NiCo-PBAs and (b) NiCo-PBAs-V in the double layer region at scanning rates of 10~100 mV s^{-1} in 1 M KOH.

References

[1] K. Wan, J. Luo, C. Zhou, T. Zhang, J. Arbiol, X. Lu, B.-W. Mao, X. Zhang, J. Fransaer, Hierarchical porous Ni_3S_4 with enriched high-valence Ni sites as a robust electrocatalyst for efficient oxygen evolution reaction, Adv. Funct. Mater., 29 (2019) 1900315.

[2] L. Lin, Q. Fu, Y. Han, J. Wang, X. Zhang, Y. Zhang, C. Hu, Z. Liu, Y. Sui, X. Wang, Fe doped skutterudite-type CoP_3 nanoneedles as efficient electrocatalysts for hydrogen and oxygen evolution in alkaline media, J. Alloys Compd., 808 (2019) 151767.

[3] Z. Kong, J. Chen, X. Wang, X. Long, X. She, D. Li, D. Yang, Cation vacancy driven efficient CoFe-LDH-based electrocatalysts for water splitting and Zn-air batteries, Mater. Adv., 2 (2021) 7932-7938.

[4] W. Zhu, X. Yue, W. Zhang, S. Yu, Y. Zhang, J. Wang, J. Wang, Nickel sulfide microsphere film on Ni foam as an efficient bifunctional electrocatalyst for overall water splitting, Chem. Commun., 52 (2016) 1486-1489.

[5] Q. Du, P. Su, Z. Cao, J. Yang, C.A.H. Price, J. Liu, Construction of N and Fe co-doped CoO/Co_xN interface for excellent OER performance, Sustain. Mater. Techno., 29 (2021) e00293.

[6] H. Yuan, S. Wang, Z. Ma, M. Kundu, B. Tang, J. Li, X. Wang, Oxygen vacancies engineered self-supported B doped Co_3O_4 nanowires as an efficient multifunctional catalyst for electrochemical water splitting and hydrolysis of sodium borohydride, Chem. Eng. J., 404 (2021) 126474.

[7] J. Sun, P. Song, H. Zhou, L. Lang, X. Shen, Y. Liu, X. Cheng, X. Fu, G. Zhu, A surface configuration strategy to hierarchical Fe-Co-S/Cu_2O/Cu electrodes for oxygen evolution in water/seawater splitting, Appl. Surf. Sci., 567 (2021) 150757.

[8] Y. Wu, J. Yang, T. Tu, W. Li, P. Zhang, Y. Zhou, J. Li, J. Li, S. Sun, Evolution of cationic vacancy defects: A motif for surface restructuration of OER precatalyst, Angew. Chem. Int. Ed., 60 (2021) 26829-26836.

[9] W. Liu, L. Yu, R. Yin, X. Xu, J. Feng, X. Jiang, D. Zheng, X. Gao, X. Gao, W. Que, P. Ruan, F. Wu, W. Shi, X. Cao, Non-3d metal modulation of a 2D Ni–Co heterostructure array as multifunctional electrocatalyst for portable overall water splitting, Small, 16 (2020) 1906775.

[10] H. Liu, X. Li, L. Chen, X. Zhu, P. Dong, M.O.L. Chee, M. Ye, Y. Guo, J. Shen, Monolithic Ni-Mo-B bifunctional electrode for large current water splitting, Adv. Funct. Mater., 32 (2022) 2107308.

[11] D. Tang, Y. Ma, Y. Liu, K. Wang, Z. Liu, W. Li, J. Li, Amorphous three-dimensional porous Co_3O_4 nanowire network toward superior OER catalysis by lithium-induced, J. Alloys Compd., 893 (2022) 162287.

[12] H. Liu, D. Zhao, M. Dai, X. Zhu, F. Qu, A. Umar, X. Wu, PEDOT decorated $CoNi_2S_4$ nanosheets electrode as bifunctional electrocatalyst for enhanced electrocatalysis, Chem. Eng. J., 428 (2022) 131183.

[13] T. Wang, X. Li, Y. Pang, X. Gao, Z. Kou, J. Tang, J. Wang, Unlocking the synergy of interface and oxygen vacancy by core-shell nickel phosphide@oxyhydroxide nanosheets arrays for accelerating alkaline oxygen evolution kinetics, Chem. Eng.

J., 425 (2021) 131491.

[14] D. Zhao, R. Zhang, M. Dai, H. Liu, W. Jian, F.Q. Bai, X. Wu, Constructing high efficiency $CoZn_xMn_{2-x}O_4$ electrocatalyst by regulating the electronic structure and surface reconstruction, Small, 18 (2022) 2107268.

[15] B. Zhong, B. Cheng, Y. Zhu, R. Ding, P. Kuang, J. Yu, Hierarchically porous nickel foam supported Fe-Ni3S2 electrode for high-current–density alkaline water splitting, J. Colloid Interf. Sci., 629 (2023) 846-853.

[16] J. Huang, Y. Sun, Y. Zhang, G. Zou, C. Yan, S. Cong, T. Lei, X. Dai, J. Guo, R. Lu, Y. Li, J. Xiong, A new member of electrocatalysts based on nickel metaphosphate nanocrystals for efficient water oxidation, Adv. Mater., 30 (2018) 1705045.

[17] G.-R. Zhang, L.-L. Shen, P. Schmatz, K. Krois, B.J.M. Etzold, Cathodic activated stainless steel mesh as a highly active electrocatalyst for the oxygen evolution reaction with self-healing possibility, J. Energy Chem., 49 (2020) 153-160.

[18] Y. Li, B. Huang, Y. Sun, M. Luo, Y. Yang, Y. Qin, L. Wang, C. Li, F. Lv, W. Zhang, S. Guo, Multimetal borides nanochains as efficient electrocatalysts for overall water splitting, Small, 15 (2019) 1804212.

[19] L. Dai, Z.-N. Chen, L. Li, P. Yin, Z. Liu, H. Zhang, Ultrathin Ni(0)-embedded $Ni(OH)_2$ heterostructured nanosheets with enhanced electrochemical overall water splitting, Adv. Mater., 32 (2020) 1906915.

[20] Y. Wen, J. Qi, P. Wei, X. Kang, X. Li, Design of Ni_3N/Co_2N heterojunctions for boosting electrocatalytic alkaline overall water splitting, J. Mater. Chem. A, 9 (2021) 10260-10269.

[21] Y. Tian, X. Xue, Y. Gu, Z. Yang, G. Hong, C. Wang, Electrodeposition of $Ni_3Se_2/MoSe_x$ as a bifunctional electrocatalyst towards highly-efficient overall water splitting, Nanoscale, 12 (2020) 23125-23133.